Widely tunable dual acousto-optic interferometric device based on a hollow core fiber

Ricardo E da Silva, Jonas H Osório, Frédéric Gérôme, Fetah Benabid, David J Webb, Marcos a R Franco, Cristiano M B Cordeiro

Optics & Laser Technology 182 (2025) 112093

Contents lists available at ScienceDirect

Optics and Laser Technology

journal homepage: www.elsevier.com/locate/optlastec

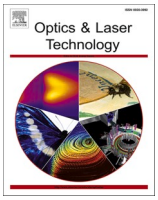

Full length article

Widely tunable dual acousto-optic interferometric device based on a hollow core fiber

Ricardo E. da Silva [a,d,*], Jonas H. Osório [b], Frédéric Gérôme [c], Fetah Benabid [c], David J. Webb [d], Marcos A.R. Franco [e], Cristiano M.B. Cordeiro [a]

[a] Institute of Physics Gleb Wataghin, University of Campinas (UNICAMP), Campinas 13083-859, Brazil
[b] Department of Physics, Federal University of Lavras (UFLA), Lavras 37200-900, Brazil
[c] GPPMM Group, XLIM Institute, UMR CNRS 7252, University of Limoges, Limoges 87060, France
[d] Aston Institute of Photonic Technologies (AIPT), Aston University, Birmingham B4 7ET, UK
[e] Institute for Advanced Studies (IEAv), São José dos Campos 12228-001, Brazil

ARTICLE INFO

Keywords:
Acousto-optic modulators
Hollow core fibers
Long period gratings
Mach-Zehnder interferometers

ABSTRACT

An all-fiber, dual Mach-Zehnder interferometer (MZI) based on an acoustically modulated hollow core fiber (HCF) is experimentally demonstrated for the first time. By attaching an acoustic driver between the fixed ends of an HCF, we fabricated two acousto-optic modulators (AOMs) with distinct driver positions, allowing synchronization of two in-line MZIs inside the HCF. The first MZI is set by two acoustic long-period gratings separated by a second MZI formed at the fiber and driver-attaching region. We show that this setup enables frequency-tuning of the coupling between the fundamental and higher-order modes in the HCF. Additionally, we simulate and analyze the HCF modal couplings and MZIs' modulated spectra under distinct device parameters using the transfer matrix method. The new AOM-MZI enables tuning of the MZI's free spectral range by adjusting 1 Hz of the electrical frequency, which is promising to modulate multiwavelength filters, sensors, and fiber lasers.

1. Introduction

All-fiber Mach-Zehnder interferometers (MZI) have successfully been applied in mode converters [1,2], fiber sensing (fuel, gas, refractive index, temperature, curvature, strain, humidity [3–11]), optical vortex beam generation [2], spectral gain flattening of fiber amplifiers [12], and multiwavelength fiber lasers [13–18]. In these devices, the input optical beam is usually split by a coupler into two beams propagating through distinct optical paths (arms). Further, these beams are recombined by a second coupler, and an interference pattern is seen at the fiber output. The free spectral range (FSR) of the interference fringes can be tuned by changing the beams' relative phase, e.g., by modifying the optical path length of one arm. With optical fibers, added flexibility can be gained by exploiting the multiple optical path lengths associated with distinct guided modes in the fiber. Additionally, distinct optical path lengths can be achieved in fiber MZIs by using concatenated-spliced fibers with special geometries (photonic crystal fibers [10,19], multicore fibers [20], suspended core fibers [9] and hollow core fibers (HCFs) [3]).

The input and output MZI couplers can be fabricated by having two localized geometric or refractive index changes over the fiber cross-section, achieved by tapering [8,11] or micro-bending [7]. Alternatively, MZIs using long-period gratings (LPGs) as couplers add spectral filtering tunability and can increase the sensitivity to external measurands [21]. In this context, the LPG notch wavelength, bandwidth, and magnitude can be tuned by adjusting the grating period and modulated refractive index amplitude. Thus, MZIs employing a pair of permanently inscribed or mechanically induced LPGs have been used in sensing and laser applications [1,2,4–6,12]. Fig. 1(a) illustrates a standard MZI composed of two LPGs inscribed in the core of a standard single-mode fiber (SMF) indicating the diameter (D) and effective length (L) of the experimental device [12]. In turn, acoustically induced LPGs couple the power of the fundamental and higher order modes, enabling tuning of the modulated notch wavelength and depth by adjusting the acoustic frequency and amplitude [22–25]. To obtain acoustically induced LPGs, one uses acousto-optic modulators (AOMs), which usually employ tapered [16,26] or etched fibers [15,17], long fibers, or high voltages (e.g., 32–38 V [24,27]) to increase the modulation efficiency.

In this framework, Fig. 1(b) illustrates an AOM-MZI employing an SMF etched 6 cm along its ends (the red triangle indicates the acoustic driver's position and the tapering transition regions are omitted for

* Corresponding author at: Institute of Physics Gleb Wataghin, University of Campinas (UNICAMP), Campinas 13083-859, Brazil.
E-mail address: resilva@unicamp.br (R.E. da Silva).

https://doi.org/10.1016/j.optlastec.2024.112093
Received 9 September 2024; Received in revised form 24 October 2024; Accepted 6 November 2024

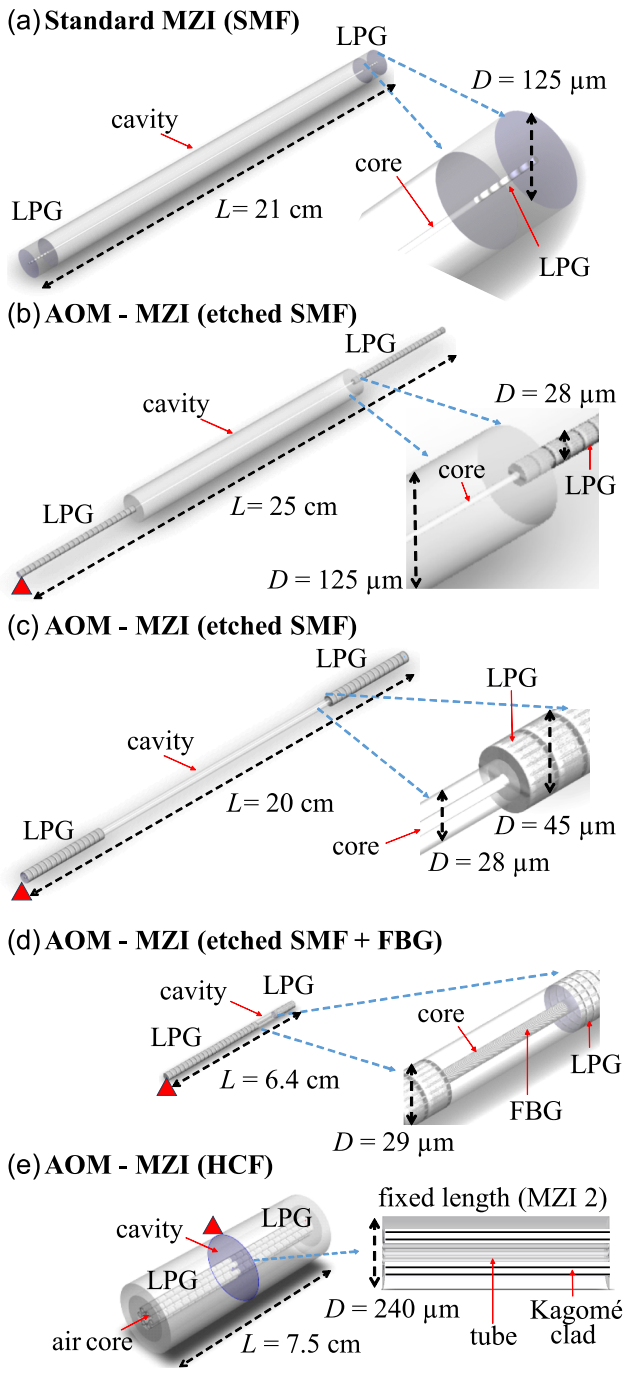

Fig. 1. Illustration of Mach-Zehnder interferometers (MZI) in different optical fiber structures employing long period gratings (LPGs), indicating their diameter (D) and effective lengths (L): (a) conventional MZI with inscribed LPGs in a standard single-mode fiber (SMF) [12], (b)(c) MZIs with acousto-optic modulated (AOM) LPGs in etched SMFs [15,17] and (d) with a fiber Bragg grating (FBG) [18], (e) AOM-MZI with a hybrid Kagomé-tubular lattice hollow core fiber (HCF) (this work).

simplicity). The generated acoustic waves exhibit higher amplitudes along the etched regions compared to the unetched fiber (a long cavity of 13 cm is required for generating multiple wavelength fringes) [15]. Additionally, MZIs with a decreased cavity diameter may be realized, as illustrated in Fig. 1(c) [17]. However, the increasing wave magnitude in the cavity might contribute to high losses and significant asymmetries in the modulated spectrum. In contrast, MZIs using uniformly etched SMFs with an inscribed fiber Bragg grating (FBG) as a cavity might provide significant AOM compactness (Fig. 1(d)) [18]. Nevertheless, the increased multimode guidance inducing evanescent power in the etched region (which is exposed to contamination from the environment) might also contribute to losses and spectral asymmetries [18]. In these approaches, FSR tuning is usually limited to small spectral phase variations induced by applied temperature or strain. Hence, the generation of multiwavelength fringes usually requires long fiber cavities in MZIs, enabling FSR tuning only by replacing components or fabricating extra devices (e.g., MZI fiber cavity lengths should be adjusted in AOMs to change the number of fringes obtained [15,26]). Thus, traditional designs based on standard fibers might also require specific fiber treatment or components, demanding extra material, fabrication time, and specialized work, which reduces the versatility and direct application of SMFs [27–29].

We have recently demonstrated highly efficient acoustically induced LPGs in tubular- and hybrid-lattice HCFs [22,23,30]. Indeed, HCF technology has experienced highly impactful advancements in recent years encompassing loss reduction, development of new fiber designs, and application demonstrations [31–34]. In this context, we experimentally demonstrate a new all-fiber AOM design comprising two in-line MZIs inside an HCF displaying a hybrid Kagomé-tubular cladding. Herein, we employed MZI configurations due to their versatility of implementation and flexibility. Indeed, these properties allow for assessing different cavity parameters and tailoring interferometric behavior, enabling the characterization of the proposed device under various excitation conditions, as described below.

The demonstrated AOMs (with centered and off-center driver positions) provide unique features to dynamically generate a multiwavelength filter by frequency-tuning the FSR in steps of 1 Hz. Fig. 1(e) illustrates the centered-driven AOM indicating details of the HCF. In addition, the modulated spectra are also simulated and studied in detail considering different MZI parameters using the transfer matrix method (TMM), as we will describe in the following sections.

2. Operation principle of the acousto-optic dual Mach-Zehnder interferometer

Acoustically induced LPGs (ALPGs) modulate the refractive index over the fiber cross-section by changing the optical path length of the guided modes due to bend-induced fiber geometric deformation. Thus, ALPGs efficiently couple the power of a mode LP_{KI} and a higher order mode LP_{MJ} at the notch wavelength λ_C when the modes' beatlength L_B phase matches with the acoustic period Λ ($L_B = \Lambda$) [16–18,22], according to,

$$\lambda_C = (n_{KI} - n_{MJ})\Lambda, \tag{1}$$

where,

$$L_B = \frac{\lambda_C}{n_{KI} - n_{MJ}}, \tag{2}$$

$$\Lambda = \left(\frac{\pi r c_{ext}}{f}\right)^{\frac{1}{2}}, \tag{3}$$

and n_{KI} and n_{MJ} are the effective refractive indices of LP_{KI} and LP_{MJ} (K, M, are the mode azimuthal numbers and, I, J, the radial numbers), r is the fiber radius, c_{ext} is the silica extensional acoustic velocity, and f is the acoustic frequency [35]. In this scenario, bend-induced axial strain changing the fiber optical path length might couple any modes having adjacent azimuthal numbers ($|K - M| = 1$), proper spatial overlap, and phase-matching as in (1) [36,37].

Fig. 2(a) illustrates the configuration we study herein, encompassing an HCF segment fixed at its ends and an acoustic driver centrally fixed along a fiber with contact length d. The acoustic driver excites simultaneously two identical ALPGs (induced by standing flexural acoustic waves of amplitude A and period Λ). We identify this configuration as

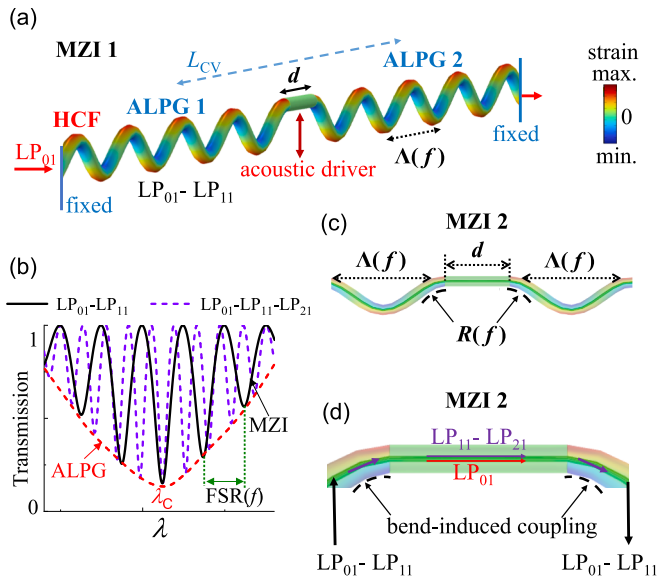

Fig. 2. (a) Illustration of a Mach–Zehnder interferometer (MZI 1) composed of two acoustically induced long period gratings (ALPG 1 and ALPG 2), excited at the central fiber length d, coupling the fundamental LP_{01} and higher order mode LP_{11} in a hollow core fiber (HCF). (b) HCF transmission spectrum tuning the fringes' free spectral range (FSR) by distinct bend-induced modal couplings in MZI 2. (c) The critical curvature radius R is changed by tuning the acoustic wave period with frequency $\Lambda(f)$. (d) MZI 2 couples higher order modes (LP_{11} and LP_{21}) increasing Δn_{eff} and the number of fringes in the spectrum in Fig. 1(b) (purple dashed line). (For interpretation of the references to colour in this figure legend, the reader is referred to the web version of this article.)

AOM – MZI 1. ALPG 1 partially couples input power confined in the fundamental mode LP_{01} to the first higher-order mode LP_{11}, modulating a notch in the HCF transmission spectrum (red line in Fig. 2(b)). The notch bandwidth of an LPG is given as [21],

$$B_W = \frac{2\lambda}{\Delta n_{eff} L_G}\sqrt{1-\left(\frac{\kappa L_G}{\pi}\right)^2}, \tag{4}$$

where, Δn_{eff} is the modes' effective refractive index difference, L_G is the grating length, and κ is the coupling coefficient (depending on the overlap of the coupled modes and modulated refractive index over the fiber cross-section). For strong LPGs where, $\kappa L_G \gg \pi$, the bandwidth in (4) can be approximated as [21],

$$B_W = \frac{2\lambda\kappa}{\pi\Delta n_{eff}}. \tag{5}$$

The maximum notch modulation depth η at λ_C can be estimated as, $\eta_{max} = sen^2(\kappa L_G)$ [21]. Thus, η and λ_C can be tuned by adjusting the acoustic amplitude A and, frequency f, respectively.

Additionally, we observe that LP_{01} and LP_{11} propagate through distinct optical path lengths along the fiber experiencing a phase shift of [5,6],

$$\phi \approx \frac{2\pi\Delta n_{eff} L_{CV}}{\lambda}, \tag{6}$$

where, λ is the optical wavelength and, L_{CV} is the ALPGs center-to-center separation (effective cavity length) [5,6,13,14]. ALPG 2 further recouples LP_{01} and LP_{11} causing them to interfere at the fiber output. The interference fringes' FSR is given by [13],

$$\text{FSR} \approx \frac{\lambda^2}{\Delta n_{eff} L_{CV}}. \tag{7}$$

Fig. 2(b) illustrates an arbitrary AOM – MZI interference spectrum caused by the coupling LP_{01} – LP_{11} (black solid line). In Fig. 2(a), we note that having d tending to zero ($d \to 0$) allows the phase matching of ALPGs 1 and 2, resulting in only one acoustic grating along the HCF. This might also occur by considerably increasing the acoustic period Λ compared to d ($\Lambda \gg d$), indicating that d should be longer than Λ to produce sufficient grating separation for the generation of multiple fringes. Alternatively, by making d smaller and comparable to Λ (e.g., $d = \Lambda/2$) and neglecting Δn_{eff} changes along d, the two gratings might work as a single ALPG with a local phase shift [1,12,38].

In this scenario, we mention that we have recently investigated flexural acoustic waves in tubular HCFs with the 3D finite element method [23]. Current studies indicate that the pressure caused by ALPGs in the fixed fiber d edges induces two strong curvatures, forming a second interferometer (MZI 2), as illustrated in Fig. 2(c). For fixed HCF ends, tuning the acoustic period with frequency $\Lambda(f)$ also tunes the critical curvature radius $R(f)$. Thus, MZI 2 similarly works as a two-point micro-bend MZI coupling higher order modes in addition to those in the ALPGs, significantly increasing n_{eff} by slightly decreasing the critical radius R [7],

$$n_{eff}(R) = n\left(1+\frac{u}{R}\right), \tag{8}$$

where, n is the unbent fiber refractive index and, u is the orientation vector from the bent fiber center. Accordingly, increasing Δn_{eff} reduces the fringes' FSR – see (7) – contributing to increasing the number of fringes in the spectrum. For example, Fig. 2(d) illustrates the coupling of LP_{11} (coming from ALPG 1) and the higher order mode LP_{21}, increasing the overall difference of optical path length compared with LP_{01}. Particularly, the coupling between the modes in the dual MZI follows the coupling sequence, $LP_{01} \to LP_{11} \to LP_{21}$ [36,37]. The resulting increased Δn_{eff} finally modulates new fringes in the HCF spectrum, as shown in Fig. 2(b) (purple dashed line). We note that MZI 2 provides a frequency-tunable multipath arm for MZI 1.

Thus, we start by analyzing the spectral characteristics of the HCF MZI and the corresponding dependences on its construction parameters by simulating it using the TMM (a detailed description of the employed formulation and modeling methods is provided in [12,19,21]). The ALPGs' parameters used in the simulations are based on the experimental components and measured modulated spectra described in the next section. Fig. 3(a) shows the HCF MZI simulated transmission spectrum indicating the acoustically modulated notches as d changes from 1.54 to 1.64 mm ($\Delta d = 100$ μm). Here, we set the acoustic driver position P to the center of the fiber length L ($P = 0.5L$) and $\Delta n_{eff} = 2.8\text{x}10^{-3}$ (in this configuration, MZI 2 modal couplings inducing multiple fringes are negligible so that $L_{CV} = d$). We note that $d = 1.54$ mm induces nearly a π-phase-shift generating two notches in the spectrum (which might also be achieved by having minor n_{eff} changes in MZI 2). In contrast, only one notch is modulated when $d = 1.64$ mm ($\phi = 2\pi$).

Additionally, Fig. 3(b) shows the results for the situation in which the driver has been further shifted to $P = 0.25L$ and $0.75L$ and the modulated spectrum evaluated at $\phi = 1\pi$ and $\phi = 2\pi$. Note that changing P is irrelevant at $\phi = 2\pi$, but the visibility of the fringes decreases for the off-center driver positions at $\phi = 1\pi$ (no difference is observed for any off-center P).

In turn, Fig. 3(c) shows the modulated spectra for increasing Δn_{eff} by about twice (black line) and 4 times (blue line) in MZI 2. As expected, the fringe number nearly doubles from $N_F \sim 7$ to 14 with decreasing FSR. For a fixed Δn_{eff}, the off-center driver would similarly reduce the fringe visibility regardless of ϕ, as seen in Fig. 3(d) and 3(e) (fringe visibility is the effective fringe magnitude or height). Overall, a proper selection of d to adjust the phase shift might be useful to equalize the magnitude of the central fringes. Fig. 3(f) shows the decreasing modulated notch bandwidth and fringe separation caused by increasing the MZI 1 length from $L = 5$ to 10 cm.

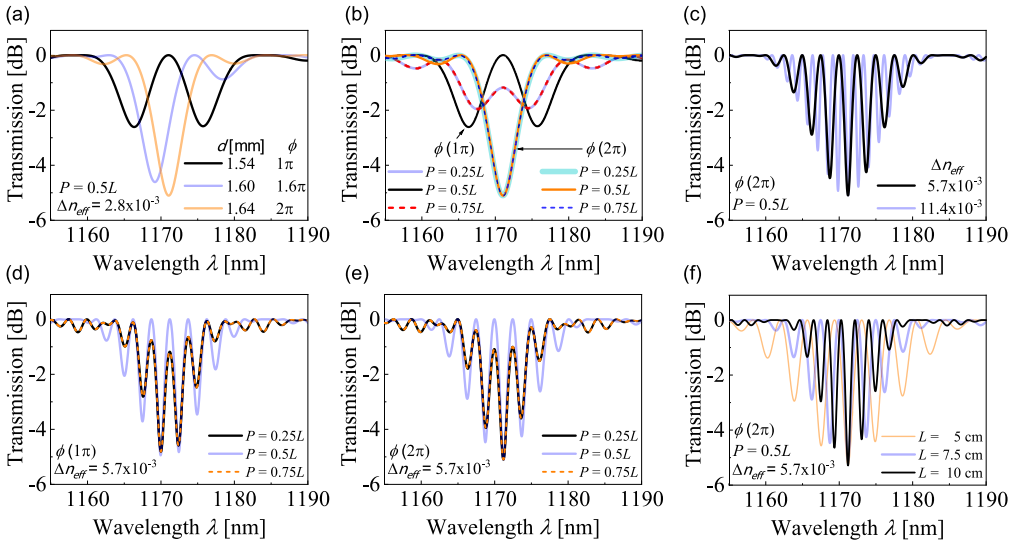

Fig. 3. HCF acoustically modulated spectra simulated with the transfer matrix method (TMM). (a) MZI 1 phase-shift variations caused by distinct fixed fiber lengths d and (b) by shifting the acoustic driver along the fiber length L at the positions $P = 0.25L$, $P = 0.5L$ and $P = 0.75L$ (for $\phi = 1\pi$ and 2π phase-shifts in Fig. 2(a)). (c) The increasing difference of the modes effective refractive index Δn_{eff} adds wavelength fringes with decreased spectral separation. The fringes visibility is reduced for off-center acoustic excitation regardless the initial phase-shift ϕ of (d) 1π or (e) 2π. (f) The modulated notch bandwidth and fringe separation are reduced by increasing the MZI 1 length from $L = 5$ to 10 cm.

3. Experimental setup

To obtain the AOMs studied here, we followed the procedure indicated in the flowchart in Fig. 4(a). The process is initiated by characterizing the HCF and AOM components for use in the experiments. This is followed by the AOM's assembly and the optical setup alignment. These steps enable the conduction of optical characterization measurements, as described in the next paragraphs.

The fabricated AOMs employ a hybrid cladding HCF composed of a Kagomé structure (800 nm strut thickness) and six suspended tubes (20 μm diameter and 1.25 μm thickness) forming the air core (34 μm diameter), as shown in Fig. 4(b). The HCF is made of silica and has a 240 μm outer diameter. Additional details about the HCF's design, fabrication, and modal characterization are described in [39].

The piezoelectric transducer disc (PZT) and horn have discrete acoustic resonances characterized by a central frequency and bandwidth at which they manifest the highest displacements, which, in turn, depend on the components' material, geometric design, and dimensions. In general, component size affects the available resonant frequencies (inverse proportionality), while the material and design affect the acoustic coupling efficiency of the generated acoustic waves and the optical fiber. Components providing matching acoustic velocities and dimensions should be most suitable to improve coupling efficiency and prevent reflections. Therefore, we have chosen a PZT and horn having dimensions and shapes that enable efficient resonant waves at low frequencies (we have previously studied other devices with similar components in the range of 50 kHz – 1 MHz, as described in [22,35]). Thus, the PZT used herein is 2 mm thick and 25 mm in diameter. The horn is tapered in diameter from 4.8 to 0.65 mm along 18 mm. When the PZT, horn, and fiber are attached, their matching resonances will define the drive frequency for the operation of the acousto-optic device, and, consequently, the wavelength step and range for tuning the modulated optical spectrum. In addition, the resulting acoustic driver will impact the modulation depth of the modulated notches and the visibility of the interferometric fringes.

Two AOMs were assembled to study the HCF's modulated transmission spectrum. Fig. 4(c) illustrates the setup of AOM 1. In turn, Fig. 4 (d) and 4(e) show representative pictures of it. The HCF ends are fixed, forming an interaction length of $L = 75$ mm, and the HCF input is butt-coupled to an SMF that is lens-coupled to a supercontinuum laser source (SC, NKT SuperK COMPACT). In sequence, the HCF output is butt-coupled to a multimode fiber (MMF) connected to an optical spectrum analyzer (OSA, Yokogawa AQ6370B). The coupling alignments are performed using micrometer stages and mirrors. Fig. 4(f) illustrates details of the dual MZI, indicating the connection of the horn and HCF. The fiber is shifted from the horn tip to increase the fiber contact length d with the horn. The horn is centered at the position, $P = 0.5L$, and fixed to the HCF with adhesive along $d \sim 1.6$ mm (red circle in Fig. 4(f)). Thus, the HCF is split into two ALPGs with equivalent lengths ($L_1 \sim L_2 \sim 36.7$ mm), forming an effective MZI 1 cavity length of $L_{CV} \sim 38.3$ mm. The separation d between the gratings corresponds approximately to MZI 2. A sinusoidal electrical signal is applied to the PZT using a signal generator (SG, HP-33120A) with a maximum voltage of 10 V (no amplifier has been used). This allows an HCF transmission spectrum notch to be obtained at $\lambda_C = 1170$ nm, tuned at $f_0 = 263.029$ kHz. The resulting fringes' FSR is tuned by adjusting the frequency from $f = 263.027$ to 263.031 kHz (1 Hz steps). A second independent experiment using the same AOM design is performed by tuning the frequency to $f_0 = 264.604$ kHz leading to a spectral notch at $\lambda_C = 1176$ nm. The FSR is then similarly tuned in 1 Hz steps from $f = 264.602$ to 264.606 kHz.

As mentioned above, we assembled a second AOM (AOM 2) employing the same components as in AOM 1. In AOM2, however, the acoustic horn is shifted 20 mm from the HCF right-end ($P \sim 0.25L$), and the ALPGs lengths are changed accordingly ($L_2 \sim 19$ mm and $L_1 \sim 54$ mm; d and L_{CV} remain with similar dimensions as in AOM 1). In this new configuration, the modulated notch at $\lambda_C = 893$ nm is set at $f_0 = 269.329$ kHz, and the fringe FSR is tuned in the range of $f = 269.327$–269.331 kHz (1 Hz step). For both experiments, the frequency tuning ranges were determined by an initial coarse tuning of f_0 in 1 kHz step to set the notch wavelength λ_C (this tuning is not continuous in the spectrum since the AOMs induce specific discrete resonances). After, a fine frequency tuning of 1 Hz defines the range of the considered FSR. Although not shown in this manuscript, other modulated notches could also be observed in the range $\lambda = 800$ to 1200 nm. The considered spectral notches have been chosen due to their interest in multiwavelength lasers, particularly around the gain range of ytterbium-doped fiber lasers [40]. The AOMs

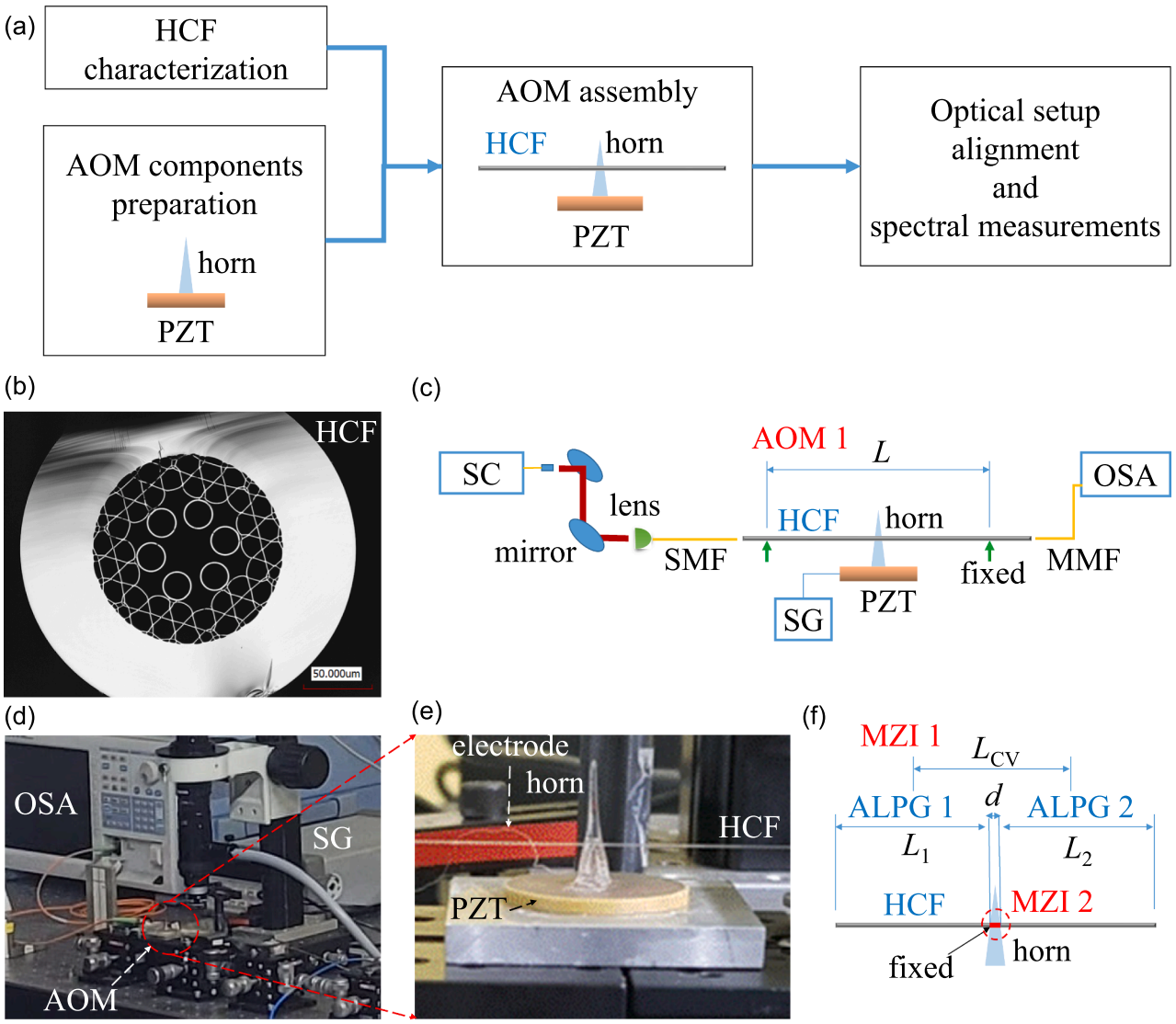

Fig. 4. (a) Flowchart indicating the steps of the experimental activities. (b) Hybrid cladding hollow core fiber (HCF). (c) Illustration and (d) representative picture of the experimental setup indicating details of the (e) acousto-optic modulator (AOM) using a piezoelectric transducer (PZT), an acoustic horn and an HCF segment of length L (horn is placed at AOM 1 center ($0.5L$) and further right-shifted in AOM 2 ($0.25L$ – not shown). (f) Details of the two Mach-Zehnder interferometers (MZIs) in AOM 1.

measured and simulated spectra are compared and analyzed in detail in Sec. IV-A and IV-B.

Additionally, we mention that the experiments have been performed under controlled room temperature conditions (20–22 °C) to prevent cross-sensitivity and influence from external temperature changes. Moreover, the employed HCF provides low sensitivity to minor temperature variations due to the large silica jacket and modal guidance confined in the air core. Other factors, such as external mechanical perturbations that could cause axially, transversally, and bend-induced strains have also been monitored. These factors might change the acoustic and optical properties causing spectral variations of the modulated fringes. In addition, power fluctuations from the laser source and misalignment of coupling components (e.g., butt-coupled fibers) might also change the modal properties inducing spectral variations. To prevent the influence of these factors, the device fiber ends (and the optical components) have been strongly fixed on XYZ stages and set to be contact-free with other devices. Furthermore, the experiment was assembled on a table with active isolation to prevent vibrations from the environment.

4. Results and discussion

4.1. FSR tuning of the multiwavelength filter with centered acoustic driver (AOM 1)

We have measured and simulated the transmission spectra of AOM 1 (centered acoustic driver configuration). Fig. 5(a) shows the simulated HCF modal beatlengths L_B compared to the acoustic period Λ calculated from the measured frequencies at $f = 263.029$ kHz and $f = 264.604$ kHz (L_B and Λ are calculated for the applied frequencies using (1)–(3) [23]). The measured notch wavelengths are indicated with vertical dashed lines in Fig. 5(a). The HCF modal effective refractive indices n_{eff} are computed by employing the actual HCF dimensions, and analytical models described in Zeisberger and Schmidt [41] (n_{eff} is computed for an arbitrary mode LP_{KI} sweeping the indices K and I from 1 to 5). Note that Λ matches simultaneously with multiple L_B (horizontal lines) indicating ALPGs couplings of the fundamental LP_{01} and higher order modes LP_{11}, LP_{21}, LP_{31}, LP_{32}, LP_{41}, and LP_{51} (this multi-coupling is caused by the modes Δn_{eff} and L_B nearly matching when λ_C approaches the edge of the HCF's transmission band [39]). The phase matching between Λ and L_B of

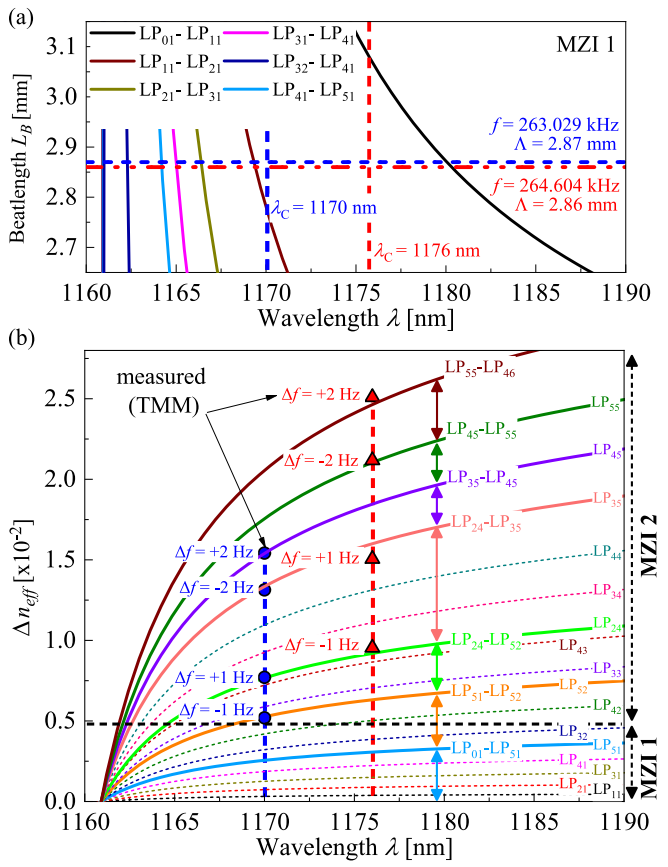

Fig. 5. (a) AOM 1 – ALPGs phase matching in MZI 1 showing the simulated HCF core modes' beatlengths L_B matching the acoustic period Λ over the measured notch bandwidth around λ_C (dashed lines). (b) Effective refractive index difference Δn_{eff} of the fundamental LP_{01} and relevant higher order modes coupling in MZI 1 and MZI 2 (main couplings are indicated with arrows and solid lines). The simulations are compared to Δn_{eff} estimated from the measured-simulated spectra for tuning frequency of $\Delta f = \pm 1$ and ± 2 Hz in Figs. 6 and 7 (blue circles and red triangles). (For interpretation of the references to colour in this figure legend, the reader is referred to the web version of this article.)

multiple modes is also observed for the second resonant notch at λ_C = 1176 nm (as indicated respectively with horizontal and vertical red lines).

Fig. 5(b) shows the modes' Δn_{eff} calculated as a difference to LP_{01}. Thus, MZI 1 couples favorably in sequence modes from LP_{01} to LP_{51} (LP_{01}-LP_{51}), as previously discussed in Sec. II. Here, only core modes with relevant spatial overlap of electric fields over the HCF cross-section are considered (details are described in Silva et al. [23]). Still, other modes with low spatial overlap (e.g., tubular modes) might also be coupled in MZI 1 with negligible modulation efficiency. These modes are therefore ignored in the simulations since they do not affect our analyses. Fig. 5(b) shows the Δn_{eff} of the modal couplings in MZI 2 (indicated by arrows and solid lines). Additionally, Fig. 5(b) displays the Δn_{eff} estimated from the measured and simulated spectra in Fig. 6 and Fig. 7 at frequency steps of $\Delta f = \pm 1$ and ± 2 Hz (blue circles and red triangles). We observe good agreement between the Δn_{eff} values, indicating FSR frequency-tuning caused by edge curvatures in MZI 2.

The measured and simulated spectra of AOM 1 for tuning frequency from f = 263.027 to 263.031 kHz are shown in Fig. 6. Fig. 6(a) shows a nearly π-phase-shift modulated spectrum indicating operation of MZI 1 at the frequency threshold of f_0 = 263.029 kHz. Fig. 6(a) shows that the ALPGs form a unique grating with a π-phase-shift induced by minor changes of the experimental fixed fiber length d (d = 1.54 mm is estimated from TMM). The modulated spectrum might also have minor Δn_{eff} changes induced in MZI 2. In contrast, a multiwavelength spectrum is achieved by slightly decreasing f to 263.028 kHz (Δf = -1 Hz), as shown in Fig. 6(b). Agreement of measured and simulated spectra implies synchronization of MZIs 1 and 2 (the flexural acoustic waves have the same polarization along the HCF in both MZIs). Additionally, we note that the measured spectrum shows high fringe visibility in Fig. 6(b).

In turn, the fringes' FSR is significantly reduced by decreasing the modulation frequency by 2 Hz, inducing new fringes in the notch (Fig. 6 (c)). Indeed, this highly sensitive FSR tuning indicates strong bend-induced intermodal coupling in MZI 2 (Fig. 5(b)). Similarly, FSR tuning is achieved by finely increasing the frequency to f = 263.030 and 263.031 kHz, as shown in Fig. 6(d) and 6(e) (fringes parameters for increasing $f(+)$ and decreasing frequency $f(-)$ are further summarized in Fig. 10, denoting slightly distinct FSR and Δn_{eff} in these cases). Moreover, reduced fringe visibility in Fig. 6(e) implies that increasing intermodal coupling might induce power loss (max. 1 dB). Overall, the average fringe FSR could be tuned from FSR = 8 to 1 nm with a tuning slope of 0.9 nm/Hz (inducing 9 fringes/Hz), as shown in Fig. 10(a) and 10(c) (f_0 spectrum is not included in FSR estimate). Additionally, we mention that the modulated spectra show a 3-dB notch bandwidth of 8 nm and an average maximum modulation depth of 4.7 dB at about λ_C = 1170 nm for the considered frequencies (except f_0). Moreover, the notch asymmetric fringe distribution around λ_C deviates from an ideal Gaussian-like profile suggesting predominant coupling of LP_{11} and LP_{21} with high field overlap [23,39] (note that the measured spectra in Fig. 6 follow closely the simulated asymmetric modal distribution shown in Fig. 5(a)).

Fig. 7 shows the modulated HCF spectra for the frequency range from f = 264.602 to 264.606 kHz (1 Hz steps). Fig. 7(a) shows the modulated notch with an intermediate phase shift tuned at the central frequency f_0 = 264.604 kHz (between 1π and 2π as seen in Fig. 3(a)), indicating a minor deviation of d in the experimental setup. The FSR is tuned from 2 to 0.7 nm by changing frequency steps of 1 and 2 Hz (1.2 and 0.4 nm/Hz slopes respectively for the negative and positive Δf). Compared to the previous modulated spectra shown in Fig. 6, the reduced FSR is expected with increasing Δn_{eff} approaching λ_C = 1176 nm (Fig. 5(b) – red triangles). The modulated notch bandwidth is 12 nm with a maximum average depth of 6 dB around λ_C = 1176 nm. The wider bandwidth B_W and higher modulation depth η might be caused by higher amplitude acoustic waves increasing the coupling coefficient κ of the modes LP_{01} and LP_{11} (Fig. 5(a) shows these modes having increased phase matching at λ_C = 1176 nm).

Observation of the data reveals reduced fringe visibility and asymmetries in the measured spectra compared to the simulations, decreasing the effective number of modulated fringes (although more fringes are seen in the simulation, only the measured central fringes are indicated in Fig. 10(c)). Eq. (5) indicates that the bandwidth B_W deviations might be caused by the significant variation of κ and Δn_{eff} with wavelength (while κ increases B_W, the modulation depth η and the visibility at λ_C, weaker couplings increase Δn_{eff} at adjacent wavelengths in MZI 2 acting to decrease B_W). Moreover, the lossy emerging higher-order modes might dissipate extra power along the edge curvatures of MZI 2 (Fig. 5(b)). Overall, reduced fringe visibility and asymmetries have also been observed in AOM-MZIs based on etched fibers and might be further minimized by increasing the applied drive voltage [16,17]. Additionally, such effects might be mitigated or controlled by employing low-loss multimode HCFs with large air holes providing increased η (fringe visibility) and smooth change of Δn_{eff} and κ over a broad spectral range.

4.2. FSR tuning of the multiwavelength filter with off-center acoustic driver (AOM 2)

We also measured and simulated the transmission spectra for the configuration involving an off-center acoustic driver (AOM 2). The results are shown in Fig. 8, where the modulated spectra are tuned in the frequency range of f = 269.327–269.331 kHz. Fig. 8(a) shows a nearly

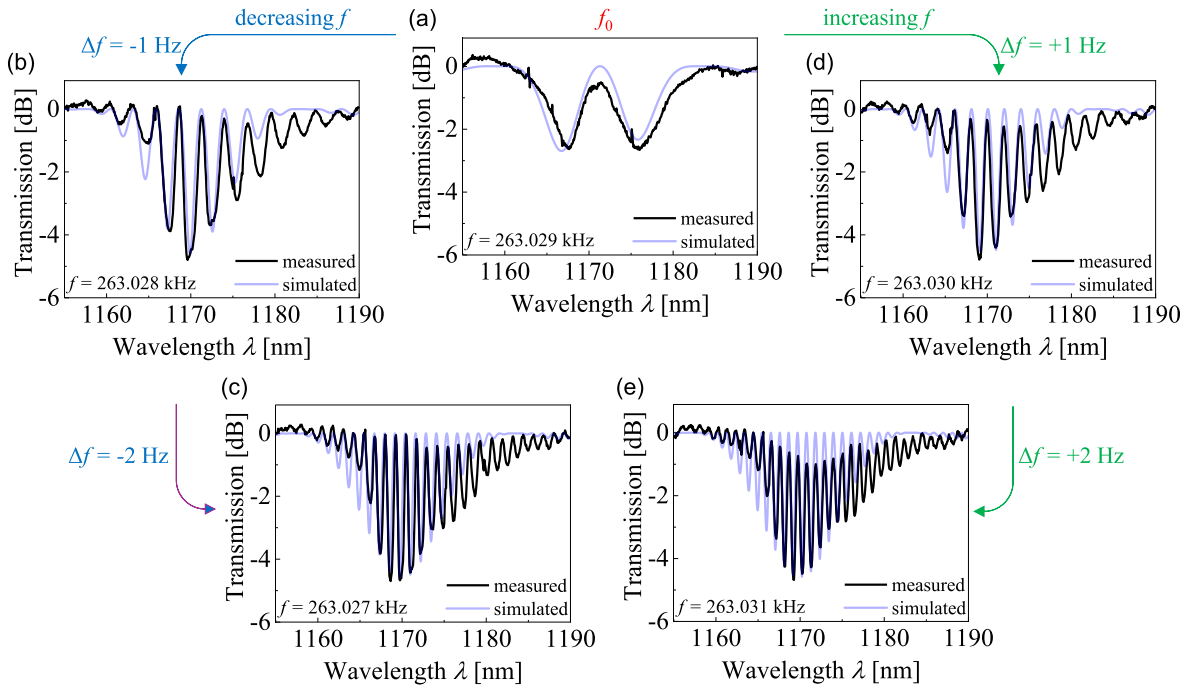

Fig. 6. AOM 1 measured and simulated transmission spectra of the hollow core fiber for the frequency range of $f = 263.027$–263.031 kHz. (a) MZI 1 induces a nearly π-phase-shift in the modulated spectrum at the threshold frequency f_0. Dual MZI multiwavelength spectra by tuning the fringes' FSR with (b)(c) decreasing frequency and (d)(e) increasing frequency respectively in steps of $\Delta f = 1$ and 2 Hz.

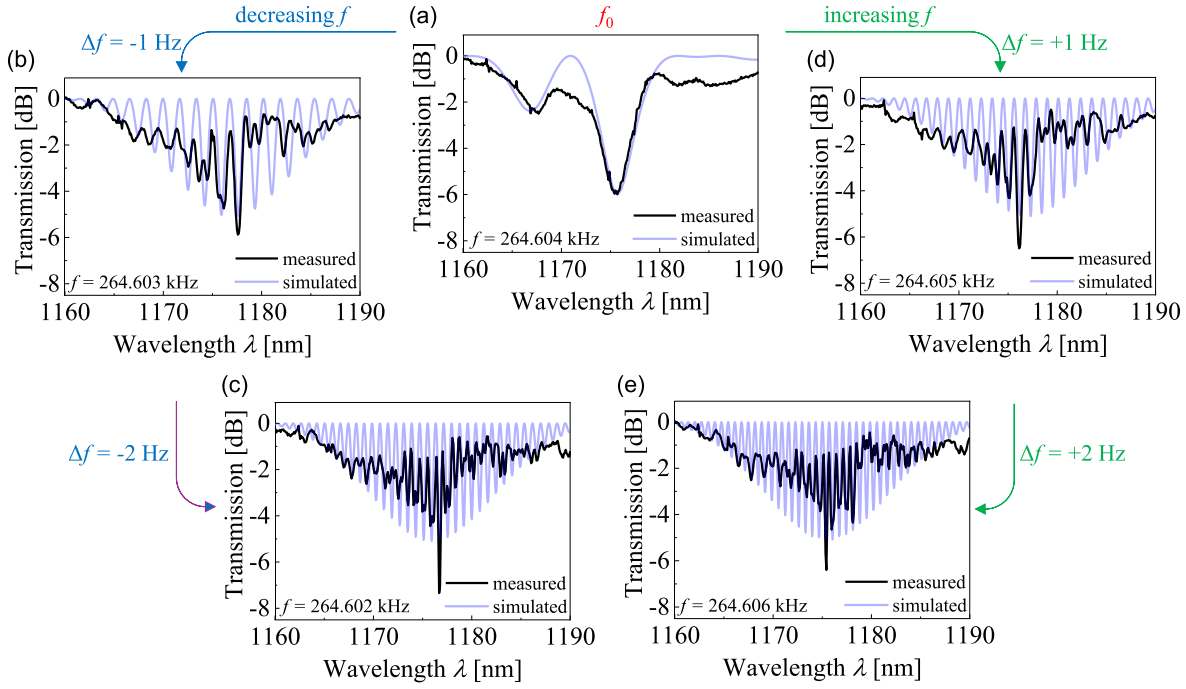

Fig. 7. AOM 1 measured and simulated transmission spectra of the hollow core fiber for the frequency range of $f = 264.602$ to 264.606 kHz. (a) MZI 1 induces a phase shift in the modulated spectrum at the threshold frequency f_0. Dual MZI multiwavelength spectra by tuning the fringes' FSR with (b)(c) decreasing frequency and (d)(e) increasing frequency respectively in steps of $\Delta f = 1$ and 2 Hz.

2π-phase-shift notch resulting from the operation of MZI 1 at $f_0 = 269.329$ kHz. In contrast to AOM 1, only one notch is observed (minor changes in d and Δn_{eff} contribute to distinct phase shifts at f_0).

Fig. 8(b) shows that a multiwavelength spectrum is generated by tuning at $f = 269.328$ kHz ($\Delta f = -1$ Hz). Observation of the data reveals that the measured and simulated fringes show decreased fringe visibility (magnitude variation of less than 1 dB) indicating the impact of having the driver at an off-center position (as expected in Fig. 3(e)). Additionally, we observe that the fringe FSR is further reduced by decreasing $\Delta f = 2$ Hz, inducing new interference fringes in the notch (Fig. 8(c)). The measured high fringe visibility indicates that increasing intermodal coupling in MZI 2 might cause a stronger effect on fringe visibility when compared to the off-center driver position (it is also noted in AOM 1). Overall, the fringe FSR is also tuned by increasing frequency, as shown

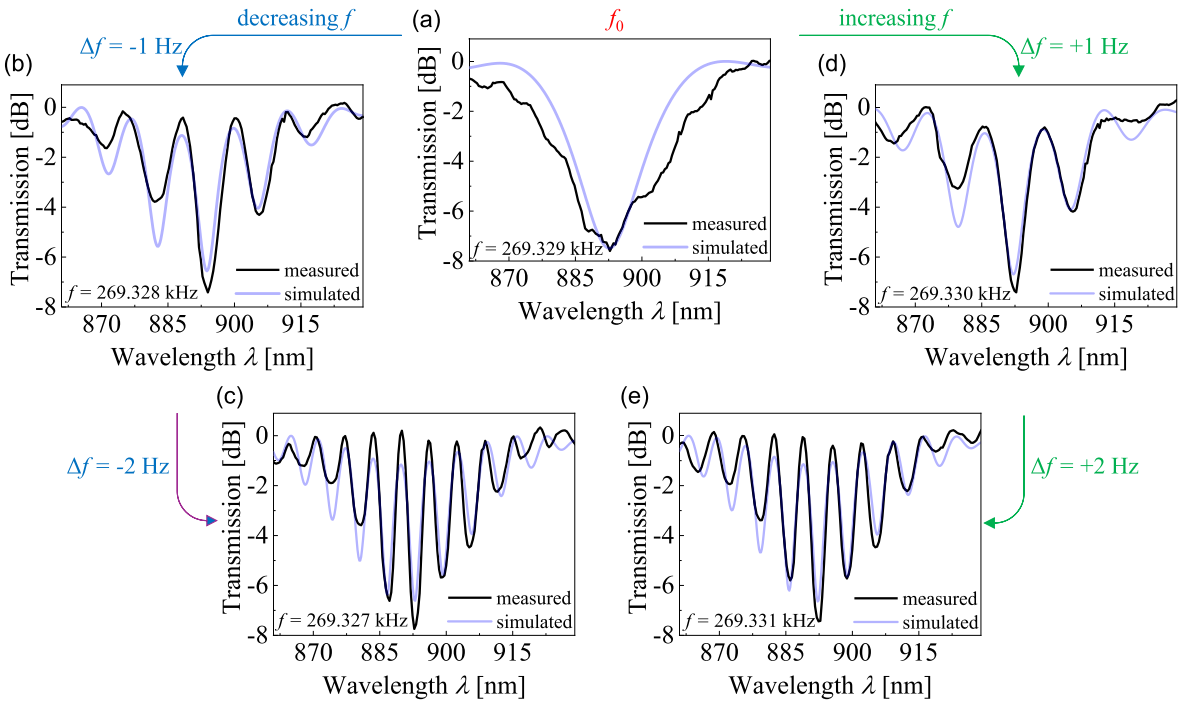

Fig. 8. AOM 2 measured and simulated transmission spectra of the hollow core fiber for the frequency range of $f = 269.327–269.331$ kHz. (a) MZI 1 induces a nearly 2π-phase-shift in the modulated spectrum at the threshold frequency f_0. Dual MZI multiwavelength spectra by tuning the fringes FSR with (b)(c) decreasing frequency and (d)(e) increasing frequency in steps of $\Delta f = 1$ and 2 Hz.

in Fig. 8(d) and (e) (note that the fringe number N_F nearly doubles at $\Delta f = +2$ Hz compared to N_F at $\Delta f = +1$ Hz). The fringes are tuned from FSR = 13 to 6 nm (average) with a slope of 6 nm/Hz (4 fringes/Hz). The tuned fringes' parameters are further summarized in Fig. 10, indicating similar FSR, N_F, and Δn_{eff} for decreasing and increasing f.

Furthermore, Fig. 8 shows that the fringe distribution in the notches is nearly symmetric around $\lambda_C = 893$ nm, resembling a Gaussian-like profile with minor phase variations. As expected, the improved notch symmetry is caused by reduced modal coupling along the ALPGs, preferentially coupling LP_{01} and LP_{11}, as indicated in Fig. 9(a) (λ_C closely matches $L_B - \Lambda$). This decreased number of couplings compared to AOM 1 is due to the larger difference between the modes Δn_{ef} as λ_C approaches the center of the HCF's transmission band [39]. In addition, Δn_{eff} changes slightly over the spectrum, also contributing to notch symmetry. This is also noted for modal coupling in MZI 2 in Fig. 9(b). The frequency-increased Δn_{eff} (blue circles) might be caused by couplings $LP_{11} - LP_{21}$ ($\Delta f = \pm 1$ Hz) and $LP_{12} - LP_{21}$ ($\Delta f = \pm 2$ Hz) (indicated with arrows and solid lines). The Δn_{eff} estimated from the measured and simulated spectra changing with frequency is shown in Fig. 10 (b) (blue line).

Overall, we note that the modulated spectra show a relevant maximum modulation depth of 7.5 dB at $\lambda_C = 893$ nm and that the notch 3-dB bandwidth changes from 24 to 28 nm (3x AOM 1 bandwidth). This improved efficiency is attributed to increased acoustically induced axial strain in the HCF tubes changing the optical guidance of modes in the air core [30]. Thus, we observe that decreasing intermodal coupling and reducing Δn_{eff} in ALPGs might be useful to broaden the notch width at the expense of having reduced fringe number, as indicated for AOM 1 and 2 in Fig. 10(c). Although we do not show it herein, we have observed increasing modulated fringes at frequencies higher than $\Delta f = 2$ Hz, suggesting that HCF modal properties might still provide broader Δn_{eff} and FSR tuning ranges by coupling modes with more similar effective refractive indices (these modes usually have high losses and do not propagate long lengths in the unbent HCF [39]).

Additionally, the modulated spectra of the AOMs showed good stability during the various experiments. The variation of the modulation depth η, FSR, and notch wavelength λ_C are characterized for AOM 2 by tuning the drive voltage from 5 to 10 V in 1 V steps at $f = 269.327$ kHz. For voltages lower than 5 V, no relevant spectral variations were noted. Fig. 11 shows the HCF's measured and simulated transmission spectra at

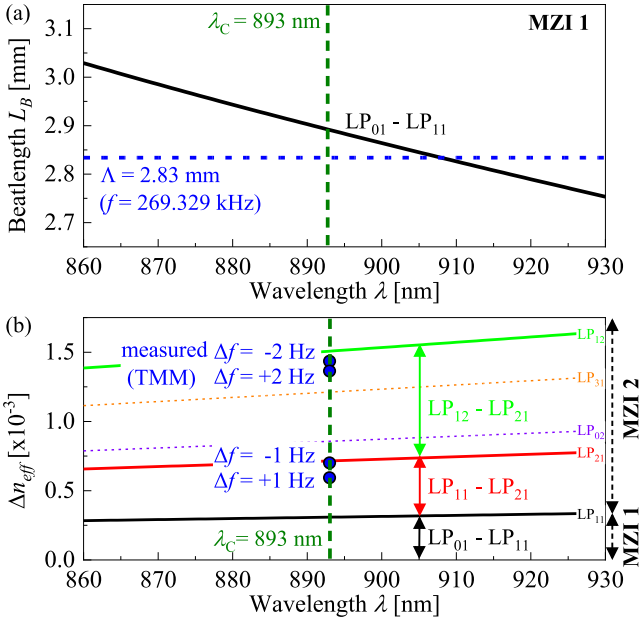

Fig. 9. (a) AOM 2 – ALPGs phase matching in MZI 1 showing the beatlength L_B of the fundamental LP_{01} and first higher order mode LP_{11} nearly matching the acoustic period Λ over the measured notch bandwidth around the λ_C. (b) Effective refractive index difference Δn_{eff} of the fundamental LP_{01} and relevant higher order modes in the HCF core. The modal couplings in MZI 1 (black arrow) and MZI 2 (red and green arrows) are compared to Δn_{eff} estimated from the measured-simulated spectra in Fig. 8 (blue circles). (For interpretation of the references to colour in this figure legend, the reader is referred to the web version of this article.)

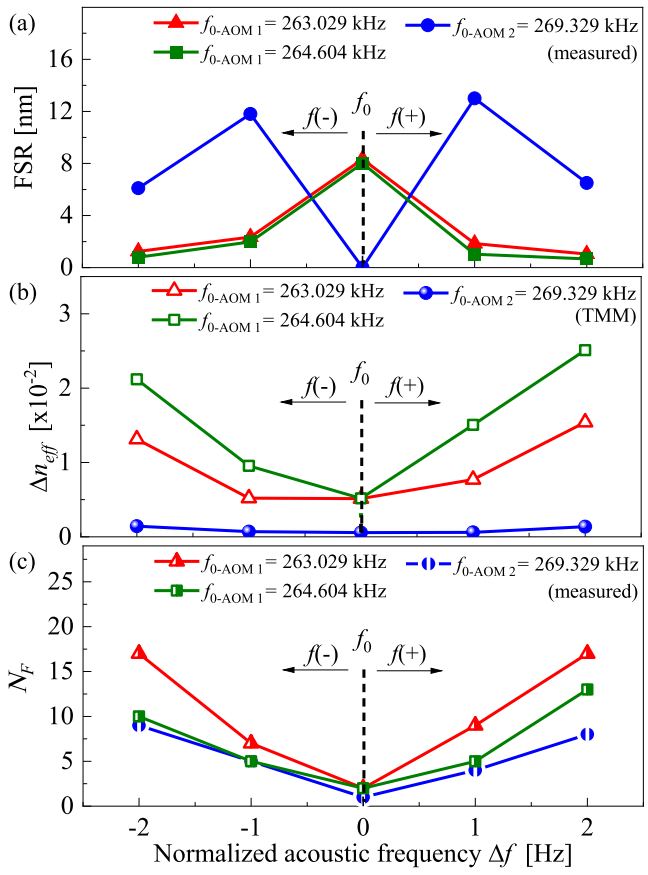

Fig. 10. AOM tuning of the fringes' (a) free spectral range (FSR), (b) modes' effective refractive index difference Δn_{eff} and the (c) fringe number N_F by decreasing f (−) and increasing f (+) the threshold frequency f_0 in 1 Hz steps (AOM 1 – red and green, AOM 2 – blue). (For interpretation of the references to colour in this figure legend, the reader is referred to the web version of this article.)

(a) 6 V, (b) 8 V, and (c) 10 V. The variation of η, FSR, and λ_C with increasing voltage is shown in Fig. 12 (ΔFSR and $\Delta\lambda_C$ are normalized in respect to the spectrum at 10 V). We note that the FSR is almost unchanged during the measurements, indicating good stability for a multiwavelength filter (minor spectral changes might come from equipment vibrations during the experiments). The FSR response indicates a stable operation of the small and fixed MZI 2 with changing acoustic wave amplitude along the ALPGs (MZI 1). The modulated spectra shift a maximum of 4.5 nm at 5 V, which is theoretically expected, since λ_C turns to higher wavelengths with increasing refractive index modulation [21] (we note that $\Delta\lambda_C$ follows the rising η in Fig. 12).

Although $\Delta\lambda_C$ shows oscillations probably caused by the non-linear behavior of the coupling interactions, the drive voltage might be useful to fine-tuning of λ_C. Overall, the increase of η with voltage demonstrates a promising almost linear response for power tuning with the AOM-MZI.

From these characterization measurements, we conclude that the demonstrated AOMs might be applied as tunable attenuators in fiber lasers, tuning the laser output by modulating the losses inside the laser cavity (lasing is then enabled at transmitted wavelengths where the gain is higher than the loss). The AOM's roles would in turn depend on the fiber laser type. For example, the AOM might be inserted into a ring laser cavity composed basically of a doped fiber (e.g., ytterbium at 1170 nm or neodymium at 890 nm) and an output coupler to deliver the power (other laser components might be required [15]). In addition, the AOMs might enable pulsed fiber lasers by modulating the acoustic wave amplitude [40]. Other important roles could arise due to the fully reconfigurable tuning of the laser's output wavelengths and power. With the considered AOM-MZI, the laser notch wavelength might be tuned by a coarse change of the acoustic frequency (kHz) while the multiwavelength FSR would be adjusted with fine steps of 1 Hz. Then, the laser power might be controlled by the applied drive voltage as demonstrated in Fig. 11.

These potential applications would highly benefit from the versatility of the MZI configuration since its operation is optically characterized in transmission, integrating external elements more easily than in other interferometric configurations. Additionally, one avoids the need for more complex arrangements or additional optical elements for light routing in configurations working in reflection [6]. Moreover, the MZI's construction parameters, such as the positioning of the acoustic horn along the fiber, can be straightforwardly adjusted, allowing for assessing different cavity parameters and tailorable interferometric behavior.

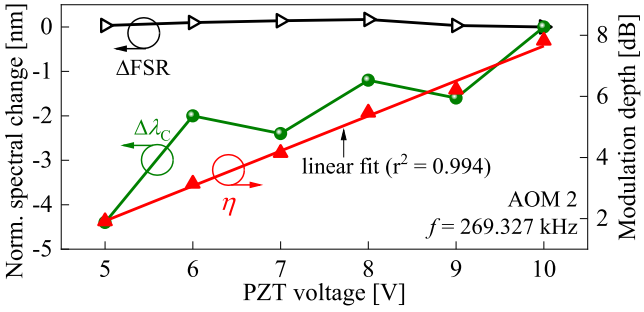

Fig. 12. Variation of the free spectral range ΔFSR, notch wavelength $\Delta\lambda_C$ and modulation depth η with increasing drive voltage from 5 to 10 V at f = 269.327 kHz (ΔFSR and $\Delta\lambda_C$ are normalized with respect to the spectrum at 10 V in Fig. 11(c)).

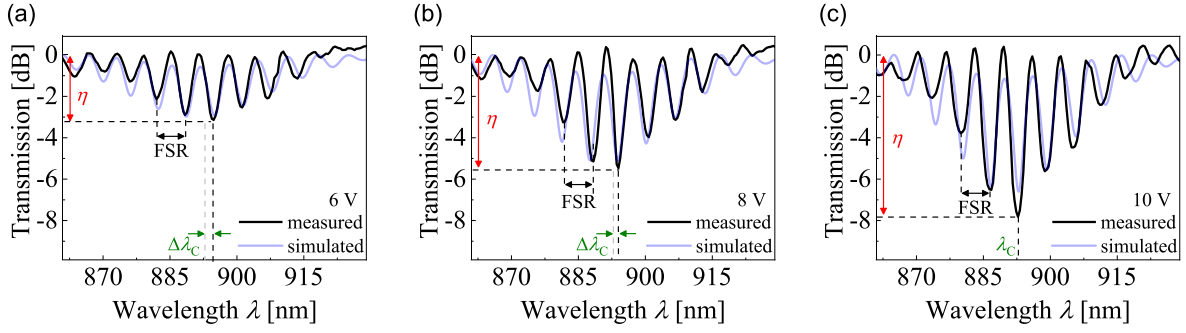

Fig. 11. AOM 2 measured and simulated transmission spectra of the hollow core fiber at the frequency of f = 269.327 kHz. The modulation depth η is tuned by changing the applied voltage to the PZT at (a) 6 V, (b) 8 V and (c) 10 V. The depth η, variation of free spectral range (ΔFSR) and of the notch wavelength $\Delta\lambda_C$ are characterized for a voltage range from 5 to 10 V in Fig. 12.

In summary, to the best of our knowledge, we demonstrated the first all-fiber acousto-optic dual MZI providing a fully reconfigurable multiwavelength filter with frequency-tunable FSR. The results indicate that changes in fringe visibility caused by changing the driver position (centered or off-center) are negligible compared to those induced by multimode coupling. Additionally, differences between measured and simulated spectra might be caused by unpredicted variations of the mode's effective indices along the HCF (e.g., caused by minor changes in the HCF geometry, dimensions, and material), as well as variations of acoustic parameters, such as ALPGs amplitude, period and length (and edge curvatures and fixed fiber length).

Additionally, the HCF intermodal coupling and modulated spectra were evaluated in detail with TMM, pointing to a powerful tool for the initial design of the dual MZI, anticipating variations of the modulated spectrum under distinct device parameters. The simulated ALPGs spectral bands (MZI 1) show phase shifts caused by changing the cavity length and position. In addition, the fringe FSR tuning with switching modal couplings and Δn_{eff} is evaluated in MZI 2. Thus, TMM has assisted in selecting the MZI components for assembly (e.g., dimensions, coupling modes and spectral range). Further, TMM has been used for analysis, evaluating results and performance of the measured spectrum (Figs. 6, 7, 8, 11), identifying modes directly inaccessible or too elaborate to be experimentally characterized, given a complex and large number of modal interactions. The deviations of measured and simulated results, such as reduced fringe visibility and notch asymmetry could be evaluated. Thus, TMM provides insights into further improvement and application of the studied devices.

Overall, the demonstrated AOM-MZI provides the following contributions and originality in comparison with the devices previously described in Fig. 1:

a) This is the first AOM-MZI based on a tubular lattice HCF (also known as antiresonant, in the literature). Considering that the acousto-optic efficiency is inversely proportional to the silica area (or fiber diameter), the Kagomé and tubular lattices (from nano to micro thicknesses) significantly reduce the silica content over the fiber cross-section, providing higher modulation efficiencies compared to solid fibers or even etched SMFs. The increased efficiency contributes to reducing the drive power (here measured in terms of a maximum 10 V voltage) preventing the need for power amplifiers and long LPG lengths.
b) The HCF provides generally lower losses and higher fringe visibility compared to previous devices by properly tuning the acoustic frequency and notch wavelength (as seen in Fig. 8). This is because the modal couplings occur mostly in the air core decreasing power dissipation in the silica components or when in contact with external agents.
c) The HCF's large silica jacket might protect the induced LPGs and modal guidance from undesired environment contamination and perturbations, providing better mechanical stability when compared to MZIs based on etched fibers.
d) The new AOM design is unique with a dual MZI that frequency-tunes the free spectral range. The acoustic driver is horizontally and vertically shifted along the fiber, and then fixed to the horn. The resulting second MZI significantly decreases the cavity length (1.6 mm) compared to devices having centimeter-scale cavities (Fig. 1). This enables a monolithic compact device (7.5 cm) with no need for concatenating etched diameters or inscription of permanent FBGs and LPGs.

Finally, we envision that further advance of this study might consider the HCF being vertically moved from the horn tip to adjust the fixed fiber length *d*. Moreover, we mention that improved modulation efficiency might still be achieved by using HCFs with larger air holes, thinner tubes, or reduced diameters, and optimizing the design of the acousto-optic device [23]. Further studies might also explore fibers with distinct geometries and materials, tailoring the spectral modal properties to improve FSR sensitivity and modulated multiwavelength spectrum. Nevertheless, to enhance the acousto-optic modulation efficiency, the doped fiber or material should have significantly reduced Young's modulus. In this case, polymer optical fibers might increase the modulation efficiency by providing higher strains compared to the silica fibers [42]. However, polymer fibers usually provide higher losses, lower acoustic velocity, and lower power-induced temperature thresholds, which limit their use in certain applications, e.g., fiber lasers. The employed HCF therefore improves the modulation efficiency while providing high power thresholds and acoustic velocities, thereby decreasing the switching time of optical devices.

5. Conclusion

We have experimentally demonstrated an all-fiber acousto-optic dual Mach–Zehnder interferometer in an HCF for the first time. The two fabricated AOMs excite a pair of dynamic ALPGs (MZI 1) separated by a transversally excited HCF segment (MZI 2). The modulated multiwavelength spectra are compared to analytical simulations using the transfer matrix method. We observed that AOM 1 (centered driver position) modulated a notch bandwidth from 8 to 12 nm with a maximum depth of 6 dB at 1176 nm. Additionally, the FSR was tuned from 8 to 0.7 nm by changing frequency steps of 1 and 2 Hz (0.9 nm/Hz slope). In turn, AOM 2 (off-center driver position) modulated a 28 nm wide notch with a maximum of 7.5 dB at 893 nm (FSR = 13–6 nm with a 6 nm/Hz slope). Thus, AOM 1 provided higher frequency-tuning sensitivity, inducing more fringes (max. 17) in a narrower asymmetric notch when compared to AOM 2, due to increased modal couplings and Δn_{eff}. In turn, AOM 2 showed a three times broader nearly symmetric notch and higher fringe visibility when compared to AOM 1. Overall, the measured and simulated spectra show that the modulated notch width, fringe number, and FSR strongly depend on the modes' refractive index difference Δn_{eff} changing with wavelength. Indeed, this property allows for the tailoring of multiwavelength filters by adjusting the HCF geometry. In conclusion, we observe that the demonstrated compact 7.5 cm long AOMs provided high modulation efficiency employing fewer components, enabling promising tuning for reconfigurable fiber sensors and lasers.

CRediT authorship contribution statement

Ricardo E. da Silva: Conceptualization, Formal analysis, Investigation, Methodology, Resources, Validation, Writing – original draft, Funding acquisition. **Jonas H. Osório:** Writing – review & editing, Resources, Methodology, Investigation, Formal analysis, Conceptualization. **Frédéric Gérôme:** Writing – review & editing, Resources. **Fetah Benabid:** Resources. **David J. Webb:** Writing – review & editing, Resources, Formal analysis. **Marcos A.R. Franco:** Writing – review & editing, Resources, Funding acquisition, Formal analysis. **Cristiano M. B. Cordeiro:** Writing – review & editing, Supervision, Resources, Investigation, Funding acquisition, Formal analysis.

Declaration of competing interest

The authors declare that they have no known competing financial interests or personal relationships that could have appeared to influence the work reported in this paper.

Acknowledgments

This work was financed, in part, by the São Paulo Research Foundation (FAPESP), Brazil [grants #2022/10584-9, #2024/02995-4]; Conselho Nacional de Desenv. Científico e Tecnológico (CNPq), Brazil [grants 305024/2023-0, 305321/2023-4]; and Minas Gerais Research Foundation (FAPEMIG), Brazil [grants RED-00046-23, APQ-00197-24].

The authors thank F. Amrani and F. Delahaye with the GPPMM Group, XLIM Institute, University of Limoges, for contributing to the fiber fabrication.

Data availability

Data will be made available on request.

References

[1] L. Zhong, Q. Huang, Q. Huang, J. Zhang, Z. Zheng, J. Li, O. Xu, O. Xu, Reconfigurable ultra-broadband mode converter based on a two-mode fiber with pressure-loaded phase-shifted long-period alloyed waveguide grating, Opt. Express 31 (2023) 8286–8295, https://doi.org/10.1364/OE.480362.

[2] Y. Zhao, Y. Zhao, Y. Zhao, Z. Liu, Y. Liu, C. Mou, T. Wang, Y. Yang, Ultra-broadband fiber mode converter based on apodized phase-shifted long-period gratings, Opt. Lett. 44 (2019) 5905–5908, https://doi.org/10.1364/OL.44.005905.

[3] K. Nazeri, F. Ahmed, V. Ahsani, H.E. Joe, C. Bradley, E. Toyserkani, M.B.G. Jun, Hollow-Core photonic crystal fiber Mach-Zehnder interferometer for gas sensing, Sensors 20 (2020) 2807, https://doi.org/10.3390/S20102807.

[4] J.H. Osório, L. Mosquera, C.J. Gouveia, C.R. Biazoli, J.G. Hayashi, P.A.S. Jorge, C. M.B. Cordeiro, High sensitivity LPG Mach-Zehnder sensor for real-time fuel conformity analysis, Meas. Sci. Technol. 24 (2012) 015102, https://doi.org/10.1088/0957-0233/24/1/015102.

[5] J.F. Ding, A.P. Zhang, L.Y. Shao, J.H. Yan, S. He, Fiber-taper seeded long-period grating pair as a highly sensitive refractive-index sensor, IEEE Photon. Technol. Lett. 17 (2005) 1247–1249, https://doi.org/10.1109/LPT.2005.847437.

[6] P. Caldas, G. Rego, Optical fiber interferometers based on arc-induced long period gratings at INESC TEC, Sensors 21 (2021) 7400, https://doi.org/10.3390/S21217400.

[7] Y. Ma, T. Tian, H. Tan, T. Geng, X. Jin, W. Sun, L. Yuan, A Mach-Zehnder interferometer with two V-shaped cores for refractive index sensing, Sens Actuators A Phys 351 (2023) 114189, https://doi.org/10.1016/J.SNA.2023.114189.

[8] T. Wei, X. Lan, H. Xiao, Fiber inline core-cladding-mode Mach-Zehnder interferometer fabricated by two-point CO_2 laser irradiations, IEEE Photon. Technol. Lett. 21 (2009) 669–671, https://doi.org/10.1109/LPT.2009.2016116.

[9] O. Frazão, S.F.O. Silva, J. Viegas, J.M. Baptista, J.L. Santos, J. Kobelke, K. Schuster, All fiber MachZehnder interferometer based on suspended twin-core fiber, IEEE Photon. Technol. Lett. 22 (2010) 1300–1302, https://doi.org/10.1109/LPT.2010.2054071.

[10] H. Young Choi, M. Jin Kim, B. Ha Lee, T.A. Birks, J.C. Knight, P.J. St Russell, R. F. Cregan, All-fiber Mach-Zehnder type interferometers formed in photonic crystal fiber, Opt. Express 15 (2007) 5711–5720, https://doi.org/10.1364/OE.15.005711.

[11] M. Shao, X. Qiao, H. Fu, N. Zhao, Q. Liu, H. Gao, An in-fiber Mach-Zehnder interferometer based on arc-induced tapers for high sensitivity humidity sensing, IEEE Sens. J. 13 (2013) 2026–2031, https://doi.org/10.1109/JSEN.2013.2247591.

[12] Y. Liu, J.A.R. Williams, L. Zhang, I. Bennion, Phase shifted and cascaded long-period fiber gratings, Opt. Commun. 164 (1999) 27–31, https://doi.org/10.1016/S0030-4018(99)00191-1.

[13] E.C. Silva-Alvarado, A. Martinez-Rios, E. Gallegos-Arellano, J.A. Martin-Vela, L. M. Ledesma-Carrillo, J.R. Reyes-Ayona, T.E. Porraz-Culebro, J.M. Sierra-Hernandez, Tunable filter based on two concatenated symmetrical long period fiber gratings as Mach-Zehnder interferometer and its fiber lasing application, Opt. Laser Technol. 149 (2022) 107824, https://doi.org/10.1016/J.OPTLASTEC.2021.107824.

[14] Y.G. Han, C.S. Kim, J.U. Kang, U.C. Paek, Y. Chung, Multiwavelength Raman fiber-ring laser based on tunable cascaded long-period fiber gratings, IEEE Photon. Technol. Lett. 15 (2003) 383–385, https://doi.org/10.1109/LPT.2002.807923.

[15] F. Gao, G. Zhang, X. Song, W. Zhang, F. Bo, J. Xu, L. Huang, P. Chang, W. Peng, Tunable in-fiber Mach-Zehnder interferometer driven by unique acoustic transducer and its application in tunable multi-wavelength laser, Opt. Express 24 (2016) 2406–2412, https://doi.org/10.1364/OE.24.002406.

[16] X. Han, F. Gao, N. Yan, G. Zhang, Z. Zhang, W. Zhang, X. Yu, J. Xu, L. Huang, P. Chang, Tunable dual-wavelength fiber laser with unique gain system based on in-fiber acousto-optic Mach-Zehnder interferometer, Opt. Express 25 (2017) 27609–27615, https://doi.org/10.1364/OE.25.027609.

[17] X. Han, Z. Wang, F. Gao, F. Gao, W. Zhang, F. Bo, X. Dong, G. Zhang, J. Xu, J. Xu, Robust and low cost in-fiber acousto-optic Mach-Zehnder interferometer and its application in a dual-wavelength laser, Appl. Opt. 61 (2022) 22–27, https://doi.org/10.1364/AO.445812.

[18] X. Han, C. Li, Y. Hu, J. Li, F. Gao, W. Zhang, X. Dong, B. Fang, G. Zhang, J. Xu, Compact dynamic in-fiber acoustically-induced Mach-Zehnder interferometer based on phase mismatch and its application in a tunable and switchable dual-wavelength laser, J. Lightwave Technol. 39 (2021) 3539–3545, https://doi.org/10.1109/JLT.2021.3067006.

[19] L. Jin, W. Jin, J. Ju, Y. Wang, Coupled local-mode theory for strongly modulated long period gratings, J. Lightwave Technol. 28 (2010) 1745–1751, https://doi.org/10.1109/JLT.2010.2049252.

[20] X. Wang, D. Chen, H. Li, G. Feng, J. Yang, In-line Mach-Zehnder interferometric sensor based on a seven-core optical fiber, IEEE Sens. J. 17 (2017) 100–104, https://doi.org/10.1109/JSEN.2016.2613018.

[21] T. Erdogan, Fiber grating spectra, J. Lightwave Technol. 15 (1997) 1277–1294, https://doi.org/10.1109/50.618322.

[22] R.E. Silva, J.H. Osório, G.L. Rodrigues, D.J. Webb, F. Gérôme, F. Benabid, C.M. B. Cordeiro, M.A.R. Franco, All-fiber broadband spectral acousto-optic modulation of a tubular-lattice hollow-core optical fiber, Opt. Lett. 49 (2024) 690–693, https://doi.org/10.1364/OL.512222.

[23] R.E. Silva, J.H. Osório, G.L. Rodrigues, D.J. Webb, F. Gérôme, F. Benabid, C.M. B. Cordeiro, M.A.R. Franco, Highly efficient interaction of a tubular-lattice hollow-core fiber and flexural acoustic waves: design, characterization and analysis, ArXiv: 2402.15825v1. https://doi.org/10.48550/arXiv.2402.15825.

[24] B.J. Miguel, H.E. Erika, N.M. Yareli, E. Rosa López, H.A. Marco, P. Olivier, D. S. Manuel, I.E. Baldemar, A. Miguel, Characterization of flexural acoustic waves in optical fibers using a fiber-tip interferometer, Meas. Sci. Technol. 35 (2024) 055206, https://doi.org/10.1088/1361-6501/AD28E9.

[25] M. Xie, J. Xu, J. Wang, H. Zhao, Y. Liu, J. Wen, F. Pang, J. Sun, A.X. Zeng, Generating broadband cylindrical vector modes based on polarization-dependent acoustically induced fiber gratings using the dispersion turning point, Photonics Res. 12 (2024) 1907–1917, https://doi.org/10.1364/PRJ.524697.

[26] W. Zhang, L. Huang, F. Gao, F. Bo, G. Zhang, J. Xu, All-fiber tunable Mach-Zehnder interferometer based on an acousto-optic tunable filter cascaded with a tapered fiber, Opt. Commun. 292 (2013) 46–48, https://doi.org/10.1016/J.OPTCOM.2012.11.057.

[27] H. Dong, H. Zhang, Y. Miao, M. Qiu, B. Liu, Spectral characteristics of single-mode-fiber-based cascaded acousto-optic filters, J. Opt. 16 (2013) 015402, https://doi.org/10.1088/2040-8978/16/1/015402.

[28] I.K. Hwang, S.H. Yun, B.Y. Kim, All-fiber tunable comb filter with nonreciprocal transmission, IEEE Photon. Technol. Lett. 10 (1998) 1437–1439, https://doi.org/10.1109/68.720286.

[29] S. Kang, H. Zhang, B. Liu, N. Zhang, Y. Miao, Acousto-optic fiber interferometer based on concatenated flexural wave modulation, Opt. Eng. 54 (2015) 076106, https://doi.org/10.1117/1.OE.54.7.076106.

[30] R.E. Silva, J.H. Osório, D.J. Webb, F. Gérôme, F. Benabid, M.A.R. Franco, C.M. B. Cordeiro, Highly efficient compact acousto-optic modulator based on a hybrid-lattice hollow core fiber, IEEE Photon. Technol. Lett. (2024), https://doi.org/10.1109/LPT.2024.3487478.

[31] Y. Chen, M.N. Petrovich, E. Numkam Fokoua, A.I. Adamu, M.R.A. Hassan, H. Sakr, R. Slavik, S.B. Gorajoobi, M. Alonso, R.F. Ando, A. Papadimopoulos, T. Varghese, D. Wu, M.F. Ando, K. Wisniowski, S.R. Sandoghchi, G.T. Jasion, D.J. Richardson, F. Poletti, Hollow core DNANF optical fiber with 0.11 dB/km loss, in: Optical Fiber Communication Conference (OFC) 2024 (2024), Paper Th4A.8, Optica Publishing Group, 2024: p. Th4A.8. 10.1364/OFC.2024.TH4A.8.

[32] J. Wahlen, M.S. Habib, O. Jones, R.A. Correa, B. Tanner, P. Ahmadi, I. Divliansky, J.E. Antonio-Lopez, M.A. Cooper, A. Schülzgen, D. Parra, S. Yerolatsitis, D. Cruz-Delgado, 2.2 kW single-mode narrow-linewidth laser delivery through a hollow-core fiber, Optica 10 (2023) 1253–1259, https://doi.org/10.1364/OPTICA.495806.

[33] Y. Hong, A. Jia, S. Gao, S. Gao, Y. Sheng, X. Lu, Z. Liang, Z. Zhang, W. Ding, Y. Wang, Y. Wang, Birefringent, low loss, and broadband semi-tube anti-resonant hollow-core fiber, Opt. Lett. 48 (2023) 163–166, https://doi.org/10.1364/OL.476126.

[34] J.H. Osório, F. Amrani, F. Delahaye, A. Dhaybi, K. Vasko, F. Melli, F. Giovanardi, D. Vandembroucq, G. Tessier, L. Vincetti, B. Debord, F. Gérôme, F. Benabid, Hollow-core fibers with reduced surface roughness and ultralow loss in the short-wavelength range, Nat. Commun. 14 (1) (2023) 1–10, https://doi.org/10.1038/s41467-023-36785-6.

[35] R.E. Silva, M.A.R. Franco, P.T. Neves, H. Bartelt, A.A.P. Pohl, Detailed analysis of the longitudinal acousto-optical resonances in a fiber Bragg modulator, Opt. Express 21 (2013) 6997–7007, https://doi.org/10.1364/OE.21.006997.

[36] X. Liu, J. Zhao, Fiber acousto-optic mode coupling between the higher-order modes with adjacent azimuthal numbers, Opt. Lett. 31 (2006) 1609–1611, https://doi.org/10.1364/OL.31.001609.

[37] S. Du-Ri, P.H. Su, K.B. Yoon, S.K. Yong, Acoustooptic generation and characterization of the higher order modes in a four-mode fiber for mode-division multiplexed transmission, J. Lightwave Technol. 32 (2014) 3932–3936. https://doi.org/10.1109/JLT.2014.2360936.

[38] H. Zhang, Y. Li, P. Zhou, H. Liu, D. Fan, C. Zhou, Experimental research of dynamic long-period fiber gratings based on ultrasound modulation, in: Optical Fibers and Sensors for Medical Diagnostics, Treatment, and Environmental Applications XXIV, SPIE (2024) 95–101. https://doi.org/10.1117/12.3000425.

[39] F. Amrani, J.H. Osório, F. Delahaye, F. Giovanardi, L. Vincetti, B. Debord, F. Gérôme, F. Benabid, Low-loss single-mode hybrid-lattice hollow-core photonic-crystal fibre, Light Sci. Appl. 10 (2021) 1–12, https://doi.org/10.1038/s41377-020-00457-7.

[40] R.E. Silva, T. Tiess, M. Becker, T. Eschrich, M. Rothhardt, M. Jäger, A.A.P. Pohl, H. Bartelt, Acousto-optic modulation of a fiber Bragg grating in suspended core fiber for mode-locked all-fiber lasers, Laser Phys. Lett. 12 (2015) 045101, https://doi.org/10.1088/1612-2011/12/4/045101.

[41] M. Zeisberger, M.A. Schmidt, Analytic model for the complex effective index of the leaky modes of tube-type anti-resonant hollow core fibers, Sci. Rep. 7 (2017) 1–13, https://doi.org/10.1038/s41598-017-12234-5.

[42] P.T. Neves Jr., A.A.P. Pohl, Time analysis of the wavelength shift in fiber Bragg gratings, J. Lightwave Technol. 25 (2007) 3580–3588, https://doi.org/10.1109/JLT.2007.907744.